The Role of Order−Disorder Transitions in the Quest for Molecular Multiferroics: Structural and Magnetic Neutron Studies of a Mixed Valence Iron(II)−Iron(III) Formate Framework

Laura Cañadillas-Delgado,[†,‡,§] Oscar Fabelo,*[,†,‡] J. Alberto Rodríguez-Velamazán,[†,‡]
Marie-Hélène Lemée-Cailleau,[‡] Sax A. Mason,[‡] Emilio Pardo,[∥] Francesc Lloret,[∥] Jiong-Peng Zhao,[⊥]
Xian-He Bu,*[,⊥] Virginie Simonet,[⊗] Claire V. Colin,[⊗] and Juan Rodríguez-Carvajal*[,‡]

[†]Instituto de Ciencia de Materiales de Aragón, CSIC-Universidad de Zaragoza, C/Pedro Cerbuna 12, E-50009, Zaragoza, Spain
[‡]Institut Laue-Langevin, 6 rue Jules Horowitz, BP 156, 38042 Grenoble Cedex 9, France
[§]Centro Universitario de la Defensa de Zaragoza. Ctra de Huesca s/n. 50090 Zaragoza, Spain
[∥]Instituto de Ciencia Molecular (ICMOL), Universitat de València, 46980 Paterna, València, Spain
[⊥]Department of Chemistry, and TKL of Metal and Molecule-Based Material Chemistry, Nankai University, Tianjin 300071, China
[⊗]Institut Néel, CNRS and UJF, BP 166, 38042 Grenoble Cedex 9, France

S *Supporting Information*

ABSTRACT: Neutron diffraction studies have been carried out to shed light on the unprecedented order−disorder phase transition (ca. 155 K) observed in the mixed-valence iron(II)−iron(III) formate framework compound $[NH_2(CH_3)_2]_n[Fe^{III}Fe^{II}(HCOO)_6]_n$. The crystal structure at 220 K was first determined from Laue diffraction data, then a second refinement at 175 K and the crystal structure determination in the low temperature phase at 45 K were done with data from the monochromatic high resolution single crystal diffractometer D19. The 45 K nuclear structure reveals that the phase transition is associated with the order−disorder of the dimethylammonium counterion that is weakly anchored in the cavities of the $[Fe^{III}Fe^{II}(HCOO)_6]_n$ framework. In the low-temperature phase, a change in space group from $P\bar{3}1c$ to $R\bar{3}c$ occurs, involving a tripling of the c-axis due to the ordering of the dimethylammonium counterion. The occurrence of this nuclear phase transition is associated with an electric transition, from paraelectric to antiferroelectric. A combination of powder and single crystal neutron diffraction measurements below the magnetic order transition (ca. 37 K) has been used to determine unequivocally the magnetic structure of this Néel N-Type ferrimagnet, proving that the ferrimagnetic behavior is due to a noncompensation of the different Fe^{II} and Fe^{III} magnetic moments.
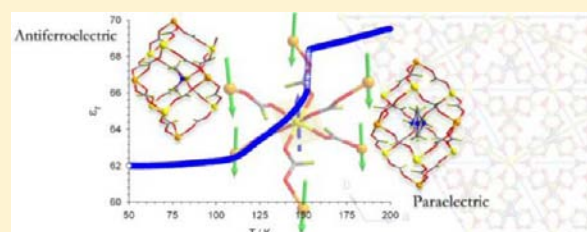
INTRODUCTION

Considerable attention is currently focused on metal−organic polymers combining two or more functionalities, for example, conductivity and magnetism,[1] magnetic and optical properties,[2] porosity and magnetism,[3] or even molecular motion and other physical properties (magnetic and electric).[4] The design of these new materials involves a wide knowledge of coordination chemistry. A large variety of organic bridging ligands which are able to efficiently transmit the magnetic exchange interactions between paramagnetic metal centers ($CN^−$, $N^{3−}$, $C_2O_4^{2−}$, $N(CN)^{2−}$, $RCOO^−$, etc.) have been extensively investigated during the last decades, and numerous compounds bridged by these ligands have been reported. The formate anion, $HCOO^−$, is the smallest and simplest carboxylate that has been observed to display multiple bridging modes. Thus, the formate ligand can adopt different bridging modes such as *syn−syn*, *anti−anti*, *syn−anti* or monatomic, and it is capable of mediating ferro- or antiferromagnetic coupling between metal ions in different situations.[5] Our interest in the formate ligand arises from its

magnetic efficiency mediating between neighboring spin carriers. Furthermore, if we can combine electrically polarizable guest molecules and a porous host lattice exhibiting magnetic order, we may, tentatively, obtain a new type of "*multiferroic*" molecular material where electric and magnetic order coexist.[6] Such multifunctional materials have recently aroused much interest from the viewpoint of the development of new materials with very large magnetoelectric effects.[7]

In this work, we focus on the previously reported $[NH_2(CH_3)_2]_n[Fe^{III}Fe^{II}(HCOO)_6]_n$ compound (**1**).[8,9] The structure of this compound was determined by single crystal X-ray diffraction, obtaining the same crystal structure at room temperature, at 173, and at 113 K.[8,9] All of them were resolved in the trigonal $P\bar{3}1c$ space group with lattice parameters close to $a = b = 8.26$ Å and $c = 13.93$ Å.[8,9] It can be described as a niccolite-like structure built up from a unique formate anion

that bridges two metal ions Fe^{III} and Fe^{II} in *anti-anti* mode giving rise to a 3D anionic framework. Charge compensation is reached through the dimethylammonium cations $[NH_2(CH_3)_2]_n$ that fill the cavities of the structure in a highly disordered manner (Figure 1, top panel).
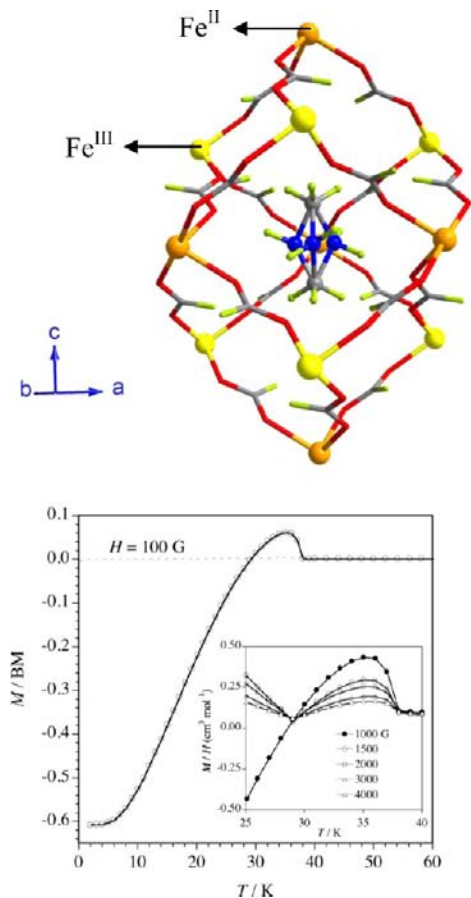
Figure 1. (Top) View of the positional disorder of the $[NH_2(CH_3)_2]$ molecule within the $[Fe^{III}Fe^{II}(HCOO)_6]_n$ cavities of the high temperature phase (1a). The Fe^{II}, Fe^{III}, oxygen, nitrogen, carbon, and hydrogen atoms are represented in orange, yellow, blue, gray, and green, respectively. (Bottom) Temperature dependence of the magnetization of a crystal of **1** (H ∥ easy axis and $H = 100$ G). The inset shows the field-cooled magnetization at different fields (H ∥ easy axis).

This compound was characterized as a Néel N-Type ferrimagnet, as reported by Hagen et al.[8] Moreover, it presents remarkable asymmetric magnetization reversal in the hysteresis loop, which was observed by Zhao et al.[9] The Néel N-Type ferrimagnet occurs when two different sublattices have different saturation magnetizations and different ordering rates with respect to temperature. The sublattice with smaller saturation magnetization orders more rapidly when the temperature decreases, and therefore, a compensation temperature (T_{comp}) should exist. The sign of the magnetization could also be negative below this compensation temperature, when the external applied field is not intense enough to rotate the magnetic moments network to achieve the alignment of the noncompensated moment along the external magnetic field (see Figure 1, bottom panel).[10] The observation of the field-cooled magnetization (FCM) with very large negative magnetization is very rare in molecule-based magnets [e.g., two-

dimensional (2D) polyiron(II,III) oxalates].[11] However, this situation is more common in the case of the ferrites (e.g., NiFe$_{2-x}$V$_x$O$_4$).[12] In any case, **1** is the first example where the negative magnetization effect is observed in a 3D molecule-based magnet.[8,9]

Herein, we report the temperature dependence of the crystal structure of the hybrid organic–inorganic niccolite-like formate $[NH_2(CH_3)_2]_n[Fe^{III}Fe^{II}(HCOO)_6]_n$. An unprecedented order–disorder phase transition compatible with an anomaly observed in the dielectric measurements has been, for the first time, observed and characterized. The neutron studies below the magnetic ordering temperature (ca. 37K) show the occurrence and evolution of long-range magnetic order.

■ EXPERIMENTAL SECTION

Physical Properties Measurement. Measurements of the heat capacity were performed using a Quantum Design Physical Properties Measurement System (PPMS), on a single crystal sample, which was mounted on the sample holder with a small amount of grease. The signal produced by this amount of vacuum grease and the sample holder was measured and subtracted.

Dielectric measurements were performed by measuring the complex impedance of the single crystal using a commercial Agilent E4980 LCR-meter.

Neutron Diffraction Measurements. Single crystal neutron diffraction experiments were carried out at the high flux reactor of the Institut Laue-Langevin (ILL, Grenoble), using the Very-Intense Vertical-Axis Laue Diffractometer (VIVALDI) as well as the D19 and D9 single-crystal monochromatic neutron diffractometers.[13]

A preliminary study was performed using Laue neutron diffraction at the VIVALDI instrument at 220 and 45 K. The comparison between the two patterns shows the appearance of new Bragg reflections in the low temperature diffraction pattern, which is a fingerprint of the occurrence of a structural phase transition. This structural change was also indicated by later specific heat measurements. The crystal structure in the high temperature phase was first refined using the Laue data (see Table 1) and later using monochromatic D19 data (see Table 1S). Since only the ratios between unit cell dimensions can be determined in the white-beam Laue technique, the low-temperature data were used only to prove the existence of a phase transition (see Figure S1, Supporting Information) which was not reported in the previous temperature dependent X-ray diffraction experiment of Zhao et al.[9] probably due to the low intensity of the X-ray superstructure reflections compared with neutron superstructure reflections.

To determine the crystal structure at 45 K, the low-temperature structural studies were carried out at the D19 instrument where the new cell parameters and the crystal structure were accurately characterized. The main crystallographic data are summarized in Table 1.

Once the crystal structure of the low-temperature phase was properly determined, the magnetic structure characterization was carried out using both neutron powder (D1B) and single crystal (D9) diffractometers. The powder measurement was made with 250 mg of ground product while the single crystal experiment was done on the same crystal as that used for the VIVALDI and D19 structural studies.

The neutron coherent scattering amplitudes used in the refinements were those tabulated by Rauch and Waschkowski.[14]

Neutron Diffraction Details. A suitable "neutron-sized" crystal with approximate dimensions of $1 \times 1 \times 3$ mm^3 was mounted on a vanadium pin. The crystal was cooled to 220 K, in a standard orange cryostat on the VIVALDI instrument. Twenty-one Laue diffraction patterns, each accumulated over 30 min, were collected every 8° in phi in two ϕ regions (rotation of the crystal about the vertical axis perpendicular to the incident beam), from −42 to −90° and from −19 to 88° in order to achieve good reciprocal space coverage as well as an adequate redundancy of equivalent reflections. The spots were indexed and processed using the program LAUEGEN,[15] and integration was performed using the program ARGONNE BOXES,[16] which uses a

Table 1. Experimental Parameters and Main Crystallographic Data for the Studied Compound

Formula	$[NH_2(CH_3)_2]_n[Fe^{III}Fe^{II}(HCOO)_6]_n$	
Empirical Formula	$C_8H_{14}Fe_2NO_{12}$	
M_r (g·mol^{-1})	427.89	
Temperature (K)	220(2)	45(2)
λ (Å)	VIVALDI,^{a} White-beam (0.80−5.20)	D19, 1.1675
Crystal system	Trigonal	Rhombohedral
Space group (No.)	$P\bar{3}1c$ (163)	$R\bar{3}c$ (167)
Crystal size (mm)	$1 \times 1 \times 3$	$1 \times 1 \times 3$
a (Å)	8.2550(12)	14.2600(17)
b (Å)	8.2550(12)	14.2600(17)
c (Å)	13.891(3)	41.443(8)
V (Å^3)	819.8(2)	7298.3(19)
Z	2	18
ρc (g·cm^{-3})	1.733	1.752
Meas. Reflections/ (Rint)	15574 (0.2526)	10926 (0.0325)
Indep. ref. $[I > 2\sigma(I)]$	713	2396
Parameters/restraints	67/0	170/0
Hydrogen treatment	Refall	Refall
Goodness of fit	1.513	1.088
Final R indices $[I > 2\sigma(I)]$: R1/wR2	0.1800/0.2635	0.0343/0.0900
R indices (all data): R1/wR2	0.2406/0.2777	0.0351/0.0905

^{a}The crystallographic details of the high temperature phase collected at the monochromatic neutron diffractometer D19 at 175 K have been provided in the Supporting Information (see text and Table 1S).

two-dimensional version of the 3D $\sigma(I)/I$ algorithm.[17] The wavelength dependent intensities were then normalized to a constant incident wavelength using the program LAUENORM.[18] The normalization process assumes that the wavelength distribution of the white neutron beam can be modeled by a high order polynomial. This approach is well adapted when the incident beam is not too perturbed between its source and the sample. In the case of VIVALDI, the presence of several monochromators upstream in the neutron guide strongly disrupts the wavelength distribution, with sharp intensity fluctuations. The subsequent calculations for structure determination were carried out using the SHELXL package.[19]

The same single crystal was mounted on the D19 diffractometer, with a neutron wavelength of 1.1675 Å from a Cu (331) monochromator at a takeoff angle of 90°.

A full data set was collected at 45 K (above the magnetic phase transition ca. 37 K) using a Displex cryorefrigerator device, after cooling at a rate of 3 K/min to avoid damage to the sample. During this cooling process, a control reflection (−1 1 −2) was scanned, and no anomaly was observed in the integrated intensities.

The cell indexing measurement protocol consisted of several 7° ω-scans with a step of 0.07°. The strong peaks were found with the ILL program PFIND and indexed with the DIRAX program;[20] the orientation matrix, the cell parameters and the chi, omega and detector offsets were postrefined with the ILL program RAFD19. After that, a sequence of approximately 80° ω-scans at a number of positions of phi and χ were collected to obtain high data completeness (3.15° < θ < 62.26° ca. 91%). The reflections were integrated using the ILL program RETREAT.[16] The crystal attenuation correction and vanadium can correction where done with the D19FACE, D19ABS and ABSCAN programs, after manually indexing the crystal faces and checking them with PLATON.[21] A similar protocol was used in the later measurement at 175K, in the high temperature phase.

The D1B instrument was operated with a wavelength of 2.521 Å, produced by a pyrolitic graphite monochromator. Graphite filters between the monochromator and the sample significantly reduce higher-order wavelength contamination, the proportion of lambda over two contamination being ca. 0.3%. The sample was contained in a Ø 3 mm cylindrical vanadium can inside an ILL orange cryostat (vanadium-tailed). The high-flux neutron patterns were collected at selected temperatures 2, 17, and 33 K, and a neutron thermodiffracto-gram between 2 and 50 K, with a heating rate of 0.1 K/min, was also

measured. The D1B data reduction was done with the LAMP software.[22]

The D9 instrument, provided with a closed-cycle cryostat, was used in the four-circle configuration with a wavelength of 0.837 Å. The program RACER[17] was used to integrate the ω-scans and to correct them for the Lorentz factor. The crystal attenuation corrections were made with the DATAP program,[23] using an estimated total neutron absorption coefficient of 1.227 cm^{-1}, essentially due to the large incoherent scattering of the hydrogen atoms.[24] The integrated intensities were collected at the same temperatures as those of the measurements at the D1B instrument.

The refinement of the magnetic structure was performed using the program FullProf[26] that allows the combined refinement of powder and single crystal data for crystal and magnetic structures using multiple diffraction patterns (multipattern refinement). The models for the magnetic structure were deduced from the output of the program BasIreps included in the FullProf Suite.

■ RESULTS AND DISCUSSION

Heat Capacity. The heat capacity shows three different peaks, which are the signature of the three phase transitions (see Figure 2). The change in heat capacity at 155 K corresponds to the paraelectric to antiferroelectric phase transition, the change at 37 K is associated with the paramagnetic−ferrimagnetic transition into Fe^{III}−Fe^{II} sublatti-ces as previously discussed,[9] while the 4.8 K signal corresponds to the low-temperature maximum observed in the relative permittivity (see next section).

The enthalpy and entropy increments, ΔH and ΔS, calculated as the areas under the C_p and C_p/T curves, respectively, were estimated at the 155 K peak as ca. 1.6 kJ mol^{-1} and 10.4 J mol^{-1} K^{-1}. The Boltzmann equation, $\Delta S = R \ln N$, where R is the gas constant and N is the ratio of the numbers of geometrically distinguishable orientations, gives $N = 3.4$. This value is close to $N = 3$ denoting three discrete states in the disordered phase, pointing to a phase transition with 3-fold order−disorder character. The well-defined signal compared with previously reported homovalence complexes[6b] indicates that the hydrogen bond network of dimethylammo-
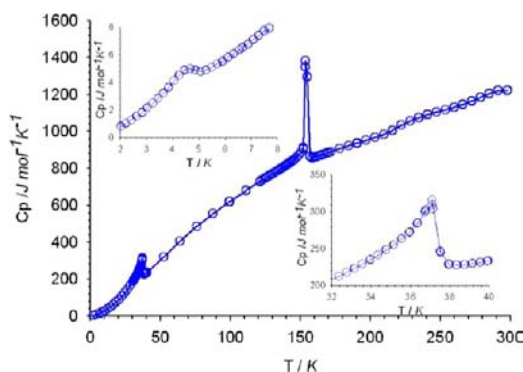
Figure 2. Heat capacity of $[NH_2(CH_3)_2]_n[Fe^{III}Fe^{II}(HCOO)_6]_n$ as a function of temperature. The insets show the detail of the λ-shaped peaks due to the paramagnetic−ferrimagnetic transition at 37 K as well as the signal observed at 4.8 K.

nium cations plays an important role in the anchorage of the dimethylammonium cations in the order−disorder phase transition.

The sharp peak associated with the paramagnetic to ferrimagnetic transition (37 K) is indicative of long-range magnetic order. The experimental magnetic entropy ($\Delta S_M = 20.4$), derived by integration of the C_p/T versus T plot from 15 to 52 K, nicely agrees with the calculated entropy for 3D magnetic ordering following the equation: $\Delta S_M = R \ln[(2s − 1)_{FeII} \times (2s − 1)_{FeIII}]$ with $s = 2$ and $s = 5/2$ for Fe^{II} and Fe^{III}, respectively.

Dielectric Measurements. The dielectric constant was measured on a single crystal with the electric field applied perpendicular to the c-axis (containing the plane of the N−H$_2$ group of the dimethylammonium cation). The dielectric constant in the form of relative permittivity (ε_r) is shown in Figure 3. The relative permittivity shows basically a linear
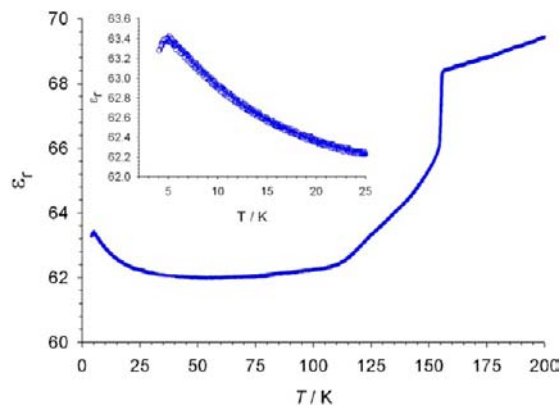
Figure 3. Relative permittivity as a function of temperature, in the range 2−50 K. The measurement was done at 10 kHz, using an amplitude of 1 V applied perpendicular to the c-axis.

decrease from 69.5 at 200 K to 68.5 at 152.8 K; then, a clear anomaly is observed as an abrupt drop from 68.5 to 66.2. The mentioned anomaly occurs in the same temperature range as that observed in the specific heat measurement (ca. 155 K), and therefore, it can be attributed to the order−disorder phase transition.

Below this transition, the permittivity value decreases in a linear way to reach a value of 62.4 at 110 K. Then, it is basically constant until ca. 40 K, and from this point, the relative

permittivity increases reaching a maximum at ca. 5.1 K. Although no modification of the magnetic structure was observed by neutron diffraction, this maximum could be related to a subtle change of the magnetic ordering, similar to the spin-canting observed in the $[NH_2(CH_3)_2]_n[Fe^{III}Mn^{II}(HCOO)_6]_n$ compound.[9] The increase of permittivity preceding this maximum starts when the magnetic order occurs. A magneto-electric effect can be discarded as the origin of this increase because the atoms responsible for the magnetic ordering are different from those responsible for the dielectric properties. Instead, a weak magnetostriction effect is observed: Figure S2 shows the variation of the lengths of the a and c axes as a function of temperature. Just below the magnetic phase transition, the values of the a and b parameters decrease slightly (relative variation of 0.1%), while the c-axis increases slightly (relative variation of 0.12%). This effect is associated with the ferrimagnetic order, responsible for the orientation of the magnetic moments mainly along the c-axis with a weak magnetic component in the ab-plane. Figure S2 also shows the variation of the lattice constant, the c/a ratio and a small increase of the cell volume in the same temperature range. Such a weak magnetostriction effect might partially account for the increase in the permittivity.

No significant hysteresis was observed in the permittivity curve between the transitions upon cooling or heating. The shape of the dielectric plot suggests that the transition at 155 K occurs from a paraelectric to an antiferroelectric phase, which is compatible with the centrosymmetric crystal structure resulting from the order−disorder structural transition. The structural phase transition corresponds to the ordering of the dimethylammonium cations at low temperature, which were initially disordered in three positions due to a 3-fold axis that passes through the carbon atoms of the dimethylammonium cation, parallel to the c-axis. This 3-fold axis is lost in the ordered phase, giving rise to a tripling of the c-axis (a detailed explanation can be consulted in the structural discussion). The angle between adjacent dimethylammonium cations along the c-axis is strictly 120°, and therefore, the resultant dipolar electric moment must be zero, producing an antiferroelectric state.

Nuclear Structure. The crystallographic studies above and below the phase transition temperature ($T \approx 155$ K) reveal for the first time a modification of the space group from $P\bar{3}1c$ [room temperature, RT, (**1a_RT**)] to $R\bar{3}c$ [low temperature, LT, (**1b_LT**)]. This structural change has not been reported before for complex 1. Keeping invariant the origin of the unit cell, in the phase transition, the a and b axes rotate 30° around the c-axis, while their values change from 8.2550(12), 8.2550(12), and 13.891(3) Å to 14.2600(17), 14.2600(17), and 41.443(8) Å for a, b, and c, respectively. The value of the c^{LT} axis is about $3 \cdot c^{RT}$, while the value of a^{LT} is very close to $3^{1/2}a^{RT}$ (see Figure 4); therefore $V^{LT} = 7290.3$ Å^3, almost equal to $9 \cdot V^{RT}$ [$P\bar{3}1c$ to $R\bar{3}c$ $a' = 2a + b$, $b' = −a + b$, $c' = 3c$].[25]

The crystal structure of complex **1a_RT** has been reported previously.[8,9] It consists of a three-dimensional network where Fe^{III}:Fe(2) and Fe^{II}:Fe(1) ions are linked by means of formate ligands along the [110], [101], and [011] directions. Each Fe^{II} ion is surrounded by six Fe^{III} neighbors, and every Fe^{III} is surrounded by six Fe^{II} ions, building in each case an octahedral arrangement around the iron ions with mixed valence.

The remaining empty space in the 3-dimensional crystal structure is about 243.6 and 2070.6 Å^3 per unit cell for **1a_RT** and **1b_LT**, respectively [29.7% (**1a_RT**) and 28.4% (**1b_LT**)
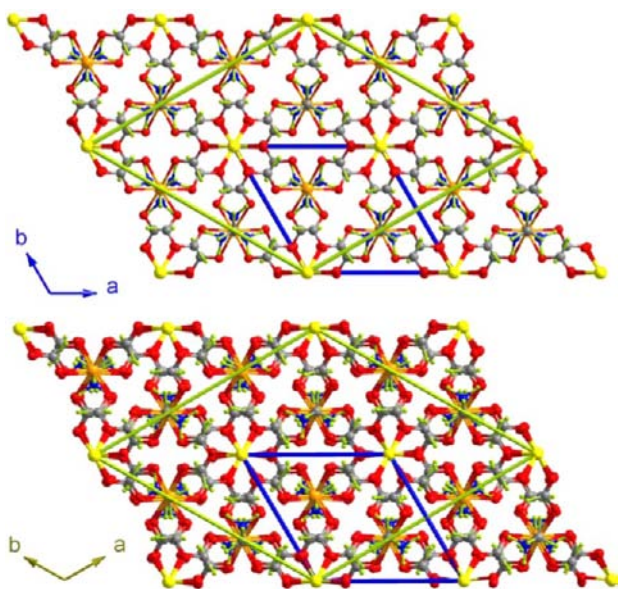
Figure 4. View along *c* axis of the **1a_RT** [top] and **1b_LT** [bottom] phases, where the **1a_RT** and **1b_LT** unit cells are represented in blue and green, respectively. The symmetry reduction is characterized by a loss of translational symmetry, the space group of phase 1a being $P\bar{3}1c$, (a, b, c), while that of phase **1b_LT** is its subgroup $R\bar{3}c$ but with unit-cell parameters $a' = 2a + b$, $b' = -a + b$, $c' = 3c$.

of the total volume], which allows the location of dimethylammonium cations in the channels. The phase transition produces slight variations in the three-dimensional lattice but more dramatic changes in the dimethylammonium cations. As mentioned before, this molecule lies in the RT structure on a 2-fold axis and a 3-fold axis, simultaneously. The 2-fold axis goes through the molecule perpendicularly through the nitrogen atom, generating the second carbon atom $C(2)^a$ [with $a = 1 - y$, $1 - x$, $0.5 - z$], while the 3-fold axis runs through the carbon atoms [$C(2)$ and $C(2)^a$] giving rise to the three positions of the nitrogen atom [$N(1)$, $N(1)^b$, and $N(1)^c$, with $b = 1 - y$, $1 + x - y$, z and $c = -x + y$, $1 - x$, z] [$N(1)-C(2)$ 1.52(3)Å]. This disorder has been reported before.[8,9] The neutron diffraction data recorded at 220 K, although of lower accuracy than data obtained from monochromatic diffraction, allowed us to locate the hydrogen atoms of the counterion. Once the structure is in the low-temperature phase, the nitrogen atom sits in a single crystallographic position since the 3-fold axis is lost giving rise to a tripling of the *c*-axis, increasing the size of the unit cell (see Figure 5), where the three independent positions of the counterion occur [$N(1)-C(1A)$ 1.491(3)Å]. The anisotropic displacement parameters of the dimethylammonium cation in this phase indicate that the molecule is not well anchored inside the cavities, but has some freedom of movement around the set positions. Hydrogen bonds involving the dimethylammonium countercation and adjacent oxygen atoms from different formate ions contribute to the stabilization of the structure (see Figure 6). The donor···acceptor/H···acceptor distances are shorter in **1b_LT**, than in **1a_RT** phase [3.042(16)/2.16(10) and 3.043(8)/
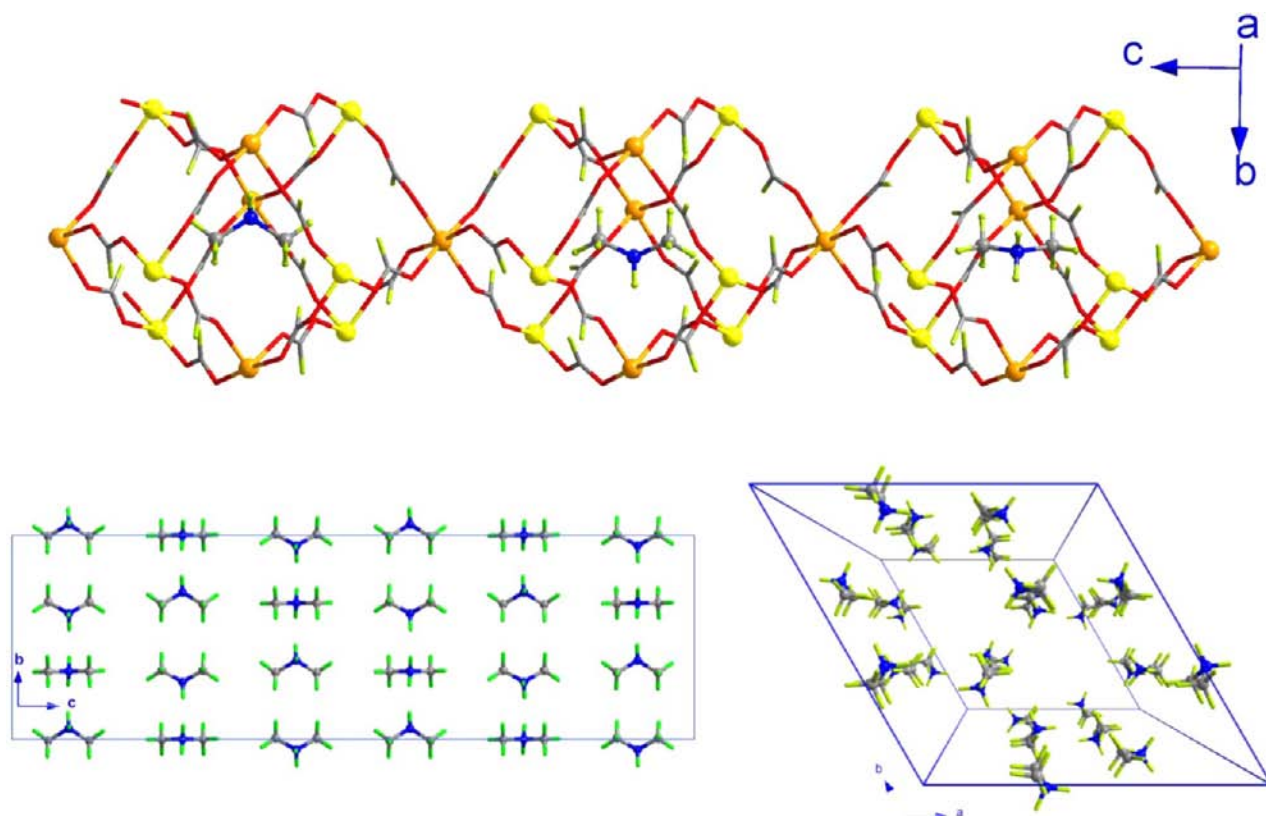
Figure 5. (Top) View of the position of the $[NH_2(CH_3)_2]$ molecule within the cavities in **1b_LT**. (Bottom-left) View along the *a*-axis of the dimethylammonium cations packing in the unit cell in the low-temperature phase. (Bottom-right) Central projection along the *c*-axis of the dimethylammonium cations inside the unit cell; note that three different positions of the dimethylammonium cations are present along the *c*-axis, due to the screw axis symmetry. The metal−organic framework has been omitted from the figure for the sake of clarity.
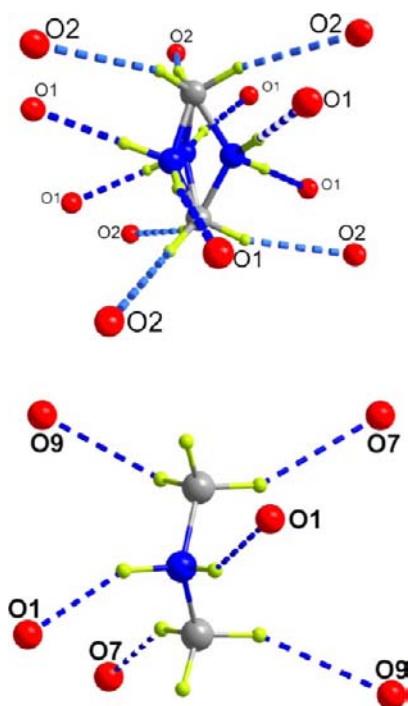
Figure 6. Detailed view of the hydrogen bonds involving the dimethylammonium countercations in **1a_RT** (top) and in **1b_LT** (bottom).

Table 2. Main Structural Variations between High and Low Temperature Phases (Distances in Angstroms)

distance	220 K	distance	45 K
Fe^{II}:Fe(1)−O	2.121(4)	Fe^{II}:Fe(1)−O(1)	2.1274(9)
		Fe^{II}:Fe(1)−O(5)	2.0875(9)
		Fe^{II}:Fe(1)−O(3)	2.1391(12)
Fe^{III}:Fe(2)−O	2.007(4)	Fe^{III}:Fe(2)−O(6)	2.0046(10)
		Fe^{III}:Fe(3)−O(4)	1.9913(10)
		Fe^{III}:Fe(3)−O(2)	2.0200(9)
C(1)−O(1)	1.238(5)	C(1)−O(1)	1.2469(10)
		C(2)−O(3)	1.2420(9)
		C(3)−O(2)	1.2407(13)
C(1)−O(2)	1.260(5)	C(1)−O(2)	1.2638(9)
		C(2)−O(4)	1.2693(13)
		C(3)−O(6)	1.2661(10)
N(1)−C(2)	1.54(4)	N(1)-C(1A)	1.491(2)
N(1)···O(1x)	3.041(9)	N(1)···O(1)	2.9198(11)
N(1)···O(1x)	3.042(2)	N(1)···O(1)	2.9214(9)

2.16(8) Å in **1a_RT** and 2.9121(9)/1.982(3) and 2.920(1)/ 1.982(3) Å in **1b_LT**].

In the **1a_RT** complex, one crystallographically independent Fe^{II}:Fe(1) and one Fe^{III}:Fe(2) are present [the Bond Valence model gives Fe^{II} 2.10 and Fe^{III} 3.07 valence units], while **1b_LT** presents one crystallographically independent Fe^{II}:Fe(1) and two Fe^{III}:Fe(2),Fe(3) [the Bond Valence model gives Fe^{II} 2.13, Fe^{III} 3.08 and 3.09 valence units]. Therefore, no significant electron transfer is expected.

In **1a_RT**, these metal ions are in an octahedral environment with just one distance defining each polyhedron [2.121(5) Å and 2.008(4) Å for Fe^{II} and Fe^{III}, respectively], in contrast with the environment of these metal ions in **1b_LT**, where just one of them [Fe(2)] is in a regular polyhedron while the other two occupy distorted polyhedra defined by different Fe−O distances [2.1274(9), 2.0875(9) and 2.1391(12) Å for Fe(1), 2.0046(7) Å for Fe(2) and 1.9919(8) and 2.0200(9) Å for Fe(3)] (see Table 2).

The small variation in distances once the **1b_LT** phase is reached means that only the Fe(2) atoms [Fe(2) also in **1a_RT**] maintain *AA* packing along the *c*-axis, while the other atoms in the 3-dimensional structure follow *ABCABC* packing, giving rise to tripling of the unit cell along this axis (see Figure 4).

The crystallographically independent formate ion in **1a_RT** exhibits a bismonodentate coordination mode which links one Fe^{II} and one Fe^{III} ion in an *anti-anti* manner. This coordination is still present in the three crystallographically independent formate ligands in **1b_LT**, but the C−O distances in the low-temperature phase are slightly lower (see Table 2).

Magnetic Structure. The magnetic structures were refined using a multipattern approach based on simultaneous refinement with powder (Rietveld method) and single-crystal (integrated intensity) data as implemented in FullProf[26] (see

Neutron Diffraction Details section). The nuclear structure determined at 45 K on the D19 instrument was taken as the structural model for the later magnetic refinement.

The neutron thermodiffractogram shows a clear increase of intensity of some Bragg reflections below 37.5 K. This feature is the signature of magnetic order, which is compatible with the magnetic behavior previously observed by macroscopic magnetometry.[8,9] The observed magnetic contribution, on top of the nuclear reflections, indicates that the magnetic reflections can be indexed with the propagation vector $\mathbf{k} = (0, 0, 0)$ (see Figure 7).
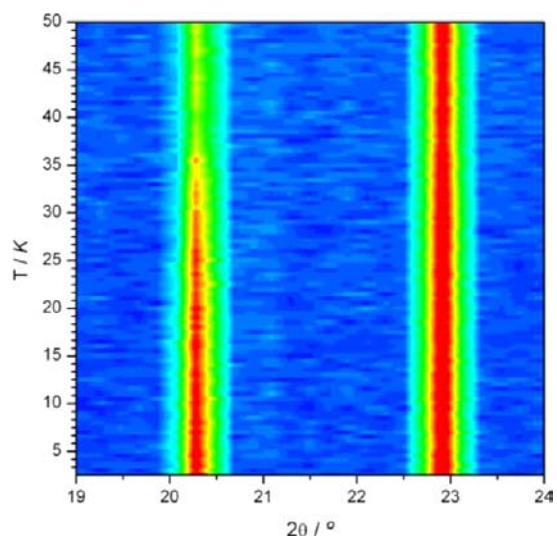
Figure 7. Detail of the mesh plot of the thermodiffractogram corresponding to $[NH_2(CH_3)_2]_n[Fe^{III}Fe^{II}(HCOO)_6]_n$ collected at D1B in the temperature range of 2−50 K, showing a clear increase of intensity at Tc (ca. 37 K) in the (110) reflection due to the occurrence of the magnetic order.

To determine the possible magnetic structures compatible with the symmetry of the crystal structure of $[NH_2(CH_3)_2]_n[Fe^{III}Fe^{II}(HCOO)_6]_n$, we have used the representational analysis techniques described by Bertaut.[27]

The propagation vector group G_k (little group) coincides with the space group $R\bar{3}c$. The six irreducible representations (irreps) of the group G_k were calculated using the program

BasIreps (included in the FullProf Suite).[28] From Γ_1 to Γ_4, all of them are one-dimensional, while Γ_5 and Γ_6 are two-dimensional. The magnetic representation Γ_M for each magnetic site [Wyckoff position 18e for Fe(1), 6b for Fe(2) and 12c for Fe(3)] can be decomposed as a direct sum of irreps by applying the great orthogonality theorem.

$$\Gamma_{18e} = \Gamma_1 \oplus \Gamma_2 \oplus 2\Gamma_3 \oplus 2\Gamma_4 \oplus 3\Gamma_5 \oplus 3\Gamma_6 \qquad (1)$$

$$\Gamma_{6b} = \Gamma_1 \oplus \Gamma_3 \oplus 2\Gamma_6 \qquad (2)$$

$$\Gamma_{12c} = \Gamma_1 \oplus \Gamma_2 \oplus \Gamma_3 \oplus \Gamma_4 \oplus 2\Gamma_5 \oplus 2\Gamma_6 \qquad (3)$$

In the present case [where $\mathbf{k} = (0, 0, 0)$], all the Fourier coefficients must be real. Therefore, the irreducible representations Γ_5 and Γ_6, which are complex, are not physically possible. If we consider that all sublattices are ordered within the same representation, the magnetic structure can only be described by irreps Γ_1 or Γ_3. This is due to the fact that Γ_2 and Γ_4 are not contained in Γ_{6b}. A detailed list of the basis vector for both possible irreducible representations (Γ_1 and Γ_3) can be consulted in Table S2.

The magnetic moments of the two possible irreps Γ_1 and Γ_3, obtained from the basis vector are shown in Table 3. The degrees of freedom are three (u, v, w) for the magnetic structure described by Γ_1, while there are four (u, v, w, p) for Γ_3.

Table 3. Magnetic Moments for the Two Possible Irreducible Representations (Γ_1 and Γ_3) of the Three Crystallographically Independent Sites[a]

| site	Γ_1	Γ_3
18e	$\mathbf{m}_{18e}(1) = \mathbf{m}_{18e}(4) = (u, u, 0)$	$\mathbf{m}_{18e}(1) = \mathbf{m}_{18e}(4) = (u, -u, v)$
	$\mathbf{m}_{18e}(2) = \mathbf{m}_{18e}(5) = (-u, 0, 0)$	$\mathbf{m}_{18e}(2) = \mathbf{m}_{18e}(5) = (u, 2u, v)$
	$\mathbf{m}_{18e}(3) = \mathbf{m}_{18e}(6) = (0, -u, 0)$	$\mathbf{m}_{18e}(3) = \mathbf{m}_{18e}(6) = (-2u, -u, v)$
6b	$\mathbf{m}_{6b}(1) = (0, 0, w)$	$\mathbf{m}_{6b}(1) = \mathbf{m}_{6b}(7) = (0, 0, w)$
	$\mathbf{m}_{6b}(7) = (0, 0, -w)$	
12c	$\mathbf{m}_{12c}(1) = \mathbf{m}_{12c}(4) = (0, 0, p)$	$\mathbf{m}_{12c}(1) = \mathbf{m}_{12c}(4) = \mathbf{m}_{12c}(7) = \mathbf{m}_{12c}(8) = (0, 0, p)$
	$\mathbf{m}_{12c}(7) = \mathbf{m}_{12c}(8) = (0, 0, -p)$	

[a]The symmetry operators are: $(1) = x, y, z$; $(2) = -y, x - y, z$; $(3) = -x + y, -x, z$; $(4) = -x, -y, -z$; $(5) = y, -x + y, -z$; $(6) = x - y, x, -z$; $(7) = y, x, -z + 1/2$; $(8) = -y, -x, z + 1/2$.

The Shubnikov group corresponding to Γ_1 is $R\bar{3}c$ and that corresponding to Γ_3 is $R\bar{3}c'$ which is compatible with antiferroelectric order. The relative orientation of the magnetic moments of site 18e is not fixed by symmetry for Γ_3 and should be determined by refining the neutron diffraction patterns. The general result will correspond to a noncollinear structure for both possible irreducible representations. The magnetic model for Γ_1 corresponds to two different networks, the 18e positions are ordered in the ab-plane while the 6b and 12c positions lie strictly along the c-axis. The Γ_3 model adds an extra degree of freedom at the 18e positions: now the magnetic moment of the Fe^{II} ions is not restricted to move in the ab-plane, and therefore, part of the magnetic moment of these ions can be coupled antiferromagnetically (AF) along the c-axis with those of Fe^{III} (occupying the 6b and 12c positions).

To elucidate the correct magnetic model, refinements of the neutron diffraction data at different temperatures (ca. 2, 17, and

33 K) were carried out using the two possible irreducible representations, Γ_1 and Γ_3. The results clearly confirm that the only possible irreducible representation compatible with the neutron diffraction data is Γ_3. With the main objective of increasing the accuracy of the refinement parameters, multi-pattern magnetic refinements at 2, 17, and 33 K were carried out with a combination of powder neutron diffraction data collected at D1B diffractometer, together with 214 Bragg reflections collected at the same temperatures on the D9 diffractometer on a single crystal sample. Figure 8 shows the best refinements ($\chi^2 = 3.61$ and $R_B = 9.89\%$ for D1B and $R_F = 6.03\%$ for D9) of the neutron data at 2 K corresponding to the Γ_3 irreducible representation. It is worth noting that some
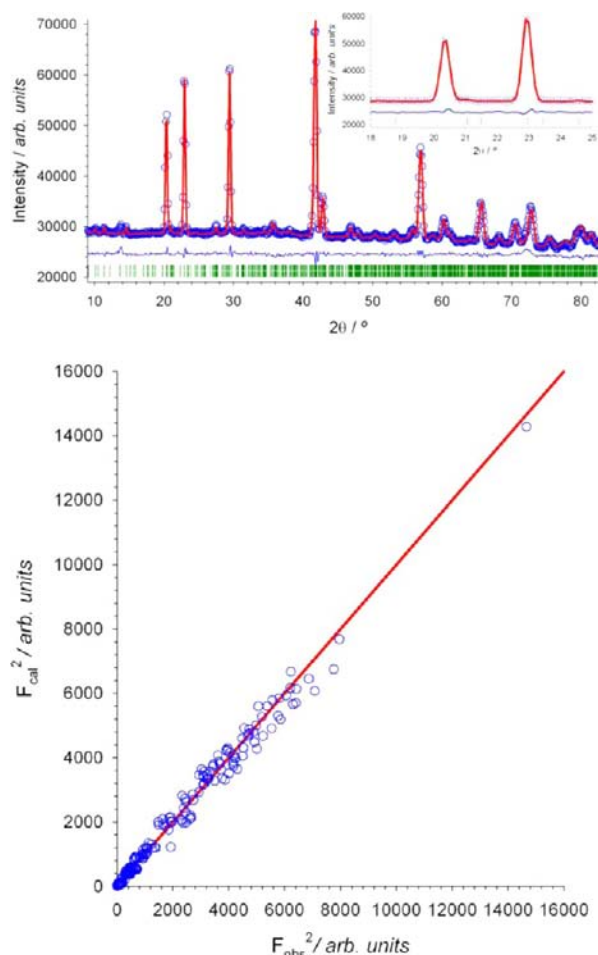
Figure 8. (Top) Experimental (blue ○) neutron diffraction data and calculated Rietveld refinement (red solid line, −) pattern for $[NH_2(CH_3)_2]_n[Fe^{III}Fe^{II}(HCOO)_6]_n$ at 2 K on D1B. The difference diffraction pattern is represented as a solid blue line (−); the markers (green vertical lines, |) indicate the position of the structural (top) and magnetic (bottom) Bragg reflections. The inset shows a detail of the data fit in the low angle region where the influence of the magnetic scattering is more pronounced. (Bottom) Plot of the observed vs calculated squared structure factors collected at 2 K at the D9 instrument. Nuclear and magnetic contributions ($F^2 = N^2 + M^2$) are included in both, observed and calculated values. The experimental data are represented as blue circles (○) and the ideal case ($F_{cal}^2 = F_{obs}^2$) is represented as a solid red line (−). The multipattern data refinement with the irreducible representations Γ_3 gives the following agreement factors $\chi^2 = 3.61$ and $R_B = 9.89\%$ for D1B and $R_F = 6.03\%$ for D9.

approximations can be made in order to reduce the number of free parameters and correlations during the refinement: due to the fact that both Fe(2) and Fe(3) are in the same oxidation state [Fe^{III}] and the magnetic moment lies along the c-axis, we assumed that $|\mathbf{m}_{6b}| = |\mathbf{m}_{12c}|$. The components of the magnetic moments within the ab-plane in the Fe(18e) site are very weak and their magnitudes have a relatively high estimated error. However, it seems that the magnetic contribution in the ab-plane is larger when the temperature increases. This suggests that the magnetic moment of the Fe^{II} ions induces a more efficient AF coupling in the network of Fe^{III} when the temperature is decreasing.

The magnetic moments of the iron ions determined by the combined refinement of the D1B and D9 data as a function of the temperature are listed in Table 4.

Table 4. Magnetic Moment Components Determined for the First Representative Iron Atom for Each of the Three Sites^{a,b}

	M_a	M_b	M_c	M_{total}
		2 K		
Fe(18e)	0.6(5)	−0.6(5)	3.8(3)	3.9(4)
Fe(6b)	0	0	−4.1(2)	−4.1(2)
Fe(12c)	0	0	−4.1(2)	−4.1(2)
		17 K		
Fe(18e)	0.7(5)	−0.7(5)	3.3(3)	3.5(4)
Fe(6b)	0	0	−3.6(3)	−3.6(3)
Fe(12c)	0	0	−3.6(3)	−3.6(3)
		33 K		
Fe(18e)	0.8(4)	−0.8(4)	2.0(5)	2.4(4)
Fe(6b)	0	0	−2.2(4)	−2.2(4)
Fe(12c)	0	0	−2.2(4)	−2.2(4)

^{a}The magnetic moment of symmetry related atoms can be obtained from the application of the basis vectors (see Table 3) as: $\mathbf{m}_{18e}$ (1) = $\mathbf{m}_{18e}$ (4) = $(u, −u, v)$, $\mathbf{m}_{18e}$ (2) = $\mathbf{m}_{18e}$ (5) = $(u, 2u, v)$ and $\mathbf{m}_{18e}$ (3) =$\mathbf{m}_{18e}$ (6) = $(−2u, −u, v)$ [with (1) = x, y, z; (2) = $−y, x − y, z$; (3) = $−x + y, −x, z$; (4) = $−x, −y, −z$; (5) = $y, −x + y, −z$; (6) = $x − y, x, −z$], $\mathbf{m}_{6b}$ (1) = $\mathbf{m}_{6b}$ (2) = $(0, 0, w)$ [with (1) = x, y, z; (2) = $y, x, −z + 1/2$] and $\mathbf{m}_{12c}$ (1) = $\mathbf{m}_{12c}$ (2) = $\mathbf{m}_{12c}$ (3) = $\mathbf{m}_{12c}$ (4) = $(0, 0, p)$ [with (1) = x, y, z; (2) = $−x, −y, −z$; (3) = $y, x, −z + 1/2$; (4) = $−y, −x, z + 1/2$]. ^{b}The components (in μ_B) are given with respect to the unit vectors along the a, b and c axes.

The spin moment of the Fe(6b) and Fe(12c) atoms lies strictly along the c-axis, while for those at the 18e position, the moment has a main component along the c-axis which is coupled antiferromagnetically with the spin moments of the 6b and 12c sites, together with a small component in the ab-plane that produces a rotation of the magnetic moments along the c-axis. As the magnetic structure is commensurate with the propagation vector $\mathbf{k} = (0, 0, 0)$, the period of repetition along the c-axis of the Fe(18e) magnetic moments is equal to the length c and the projection of the angle of rotation of these moments in the ab-plane is strictly 120° (screw axis 3$_1$ or 3$_2$). Therefore, after three translations along the c-axis, the magnetic moments of the Fe(18e) ions will be in the initial conformation (see Figure 9a,b). This model produces a ferrimagnetic layered structure, where the magnetic moments follow an AA packing sequence for the layers containing Fe^{III} ions (blue arrows in Figure 9c,d) and a $ABCDEFA$ sequence for the layers containing Fe^{II} ions (green arrows in Figure 9c,d); as a consequence, the Fe^{II} layers are not repeated inside the unit cell.
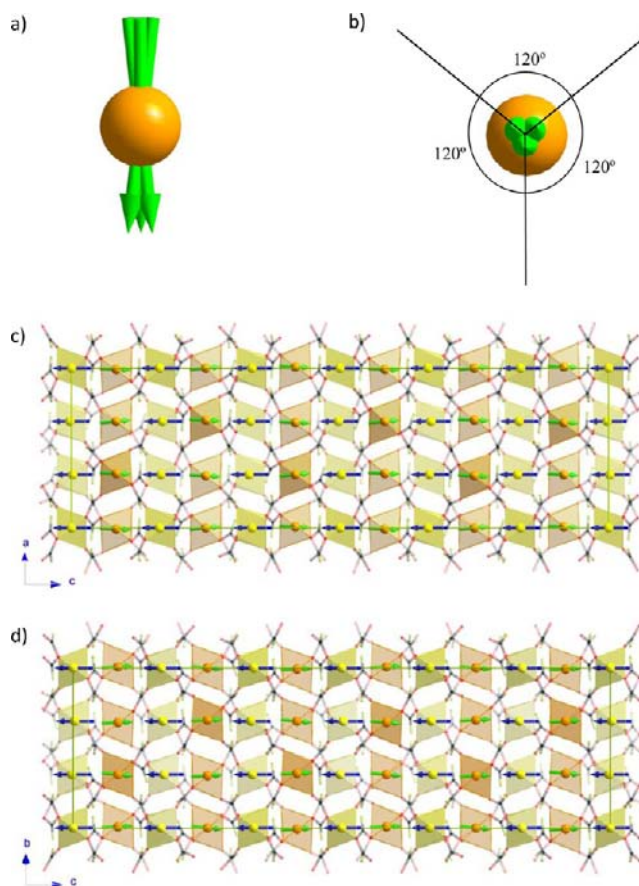
Figure 9. (a) View perpendicular to the c-axis of the projection of the magnetic moment of three adjacent Fe^{II} atoms at the central Fe(18e) site. (b) Perspective view along the c-axis of the same projection, where the angles between the moments projected in the ab-plane have been represented. (c) View along the b-axis of the unit cell of $[NH_2(CH_3)_2]_n[Fe^{III}Fe^{II}(HCOO)_6]_n$ together with the magnetic moment of each Fe^{II} and Fe^{III} site, yellow/blue and orange/green, for nuclear/magnetic structure, respectively. (d) Perspective along the a-axis of the nuclear and magnetic structure of $[NH_2(CH_3)_2]_n[Fe^{III}Fe^{II}(HCOO)_6]_n$, color code as in (c). The formate ligands have been represented in transparent mode; the dimethylammonium cations have been omitted for the sake of clarity.

The ferrimagnetic moment (μ_f), which arises as a result of the noncompensation of the Fe^{II}−Fe^{III} sublattices, is calculated as the vector sum of the magnetic moments obtained from the neutron measurement at 2 K along the c-axis, ca. 0.3 μ_B. This value is slightly lower than that obtained experimentally by using a Magnetic Properties Measurement System (MPMS-SQUID) (0.6 μ_B).[9] It should be noted that the present neutron diffraction experiments give information only about the magnetic moment resident on the iron sites and not about that delocalized out of them. To analyze the magnitude of the magnetic moments over the magnetic and the nonmagnetic atoms as well as the distribution of the spin density in the organic linkers, polarized neutron diffraction experiments might be of interest.

CONCLUSIONS

In this work, we present the crystal and magnetic structures of the compound $[NH_2(CH_3)_2]_n[Fe^{III}Fe^{II}(HCOO)_6]_n$ obtained from neutron diffraction techniques. The Laue neutron diffraction studies at 220 K allowed the determination of the

hydrogen position of the dimethylammonium cations, which was not possible in the previous X-ray model.[8,9] The crystal structure below the structural phase transition has also been determined using monochromatic neutron diffraction at the D19 single crystal diffractometer. The transformation of the space group from $P\bar{3}1c$ to $R\bar{3}c$ has been completely characterized. This transformation implies a tripling of the c-axis which is associated with the ordering of the dimethylammonium countercations: in the high-temperature phase, the dimethylammonium is disordered over three different positions, and once the temperature is below the nuclear phase transition, the dimethylammonium cations are well ordered into three different positions related by the 3-fold screw axis lying along the c-axis. The order–disorder phase transition is triggered by the occurrence of an extensive network of hydrogen bonds, involving dimethylammonium hydrogen atoms as donors and oxygen atoms from the carboxylate group as acceptors. This feature is important for the interpretation of the electric properties. The measurement of the temperature dependence of the relative permittivity shows an electric transition, which has been assigned to a paraelectric to antiferroelectric phase transition. This transition occurs simultaneously to the crystallographic one, and therefore, it is triggered by the order–disorder transition of the dimethylammonium counterions. Below the Curie temperature, a slight variation of the dielectric properties coincides with the onset of the magnetic order and a possible spin reorientation.

The refined magnetic structure below 37 K corresponds to a weakly noncollinear ferrimagnetic structure, where the Fe^{II} and Fe^{III} sites are antiferromagnetically coupled.

From the magnetization study, a compensation temperature, T_{comp}, was observed at ca. 29 K (Figure 1). As can be seen from Table 4, at 33 K (above T_{comp}), the magnetization value of the Fe^{III} site is lower than that of Fe^{II} (−2.20 and +2.40 μ_B, respectively), while at 17 K (below T_{comp}), the opposite situation occurs (−3.6 and +3.5 μ_B). These data also suggest that the Fe^{II} sublattice is the first one to be ordered and then induces the Fe^{III} sublattice to be coupled antiferromagnetically with it. Below this T_{comp}, the proportion of the ordered magnetic moment increases more noticeably for the Fe^{III} sublattice, consistently with a Néel N-Type ferrimagnet, and a negative magnetization is observed. It is worth noting that the value of magnetization at 2 K for the Fe^{II} sublattice is close to the ideal value ca. 97.5% of the saturation value; however, the value for the Fe^{III} sublattice is far from saturation (ca. 82%). This notable difference of magnetic moment can be due to a combination of geometrical distortion and/or strong covalence effects.

In summary, the inclusion of different polar molecules within a magnetic metal–organic framework for the design of molecular materials combining magnetic and electric ordering appears as a promising strategy to be extensively explored.

ASSOCIATED CONTENT

ⓈSupporting Information

Dielectric measurements details. Crystallographic details of data collected at the monochromatic neutron diffractometer D19 at 175 K. Image-plate neutron diffraction pattern collected at the VIVALDI instrument at 220 and 45 K. Graphical representation of the temperature variation of the lattice parameters, volume and c/a ratio. Table of basis vectors of the two possible irreducible representations (Γ_1 and Γ_3). The Laue (220 K) and monochromatic (175 and 45 K) neutron data in CIF format.

This material is available free of charge via the Internet at http://pubs.acs.org.

AUTHOR INFORMATION

Corresponding Author

fabelo@ill.fr; buxh@nankai.edu.cn; jrc@ill.fr

Notes

The authors declare no competing financial interest.

ACKNOWLEDGMENTS

REFERENCES

(1) (a) Coronado, E.; Galan-Máscarós, J. R.; Gómez-García, C. J.; Laukhin, V. *Nature* **2000**, *408*, 447. (b) Kurmoo, M.; Graham, A. W.; Day, P.; Coles, S. J.; Hursthouse, M. B.; Caulfield, J. L.; Singleton, J.; Pratt, F. L.; Hayes, W.; Ducasse, L.; Guioneau, P. *J. Am. Chem. Soc.* **1995**, *117*, 12209. (c) Coronado, E.; Day, P. *Chem. Rev.* **2004**, *104*, 5419. (d) Uji, S.; Shinagawa, H.; Terashima, T.; Yakabe, T.; Terai, Y.; Tokumoto, M.; Kobayashi, A.; Tanaka, H.; Kobayashi, H. *Nature* **2001**, *410*, 908. (e) Kobayashi, H.; Cui, H.-B.; Kobayashi, A. *Chem. Rev.* **2004**, *104*, 5265.

(2) (a) Sato, O. *Acc. Chem. Res.* **2003**, *36*, 692. (b) Sunatsuki, Y.; Ikuta, Y.; Matsumoto, N.; Ohta, H.; Kojima, M.; Iijima, S.; Hayami, S.; Maeda, Y.; Kaizaki, S.; Dahan, F.; Tuchagues, J. P. *Angew. Chem., Int. Ed.* **2003**, *42*, 1614. (c) Lacroix, P. G.; Malfant, I.; Bénard, S.; Yu, P.; Rivière, E.; Nakatani, K. *Chem. Mater.* **2001**, *13*, 441. (d) Evans, J. S. O.; Bénard, S.; Yu, P.; Clément, R. *Chem. Mater.* **2001**, *13*, 3813.

(3) (a) Maspoch, D.; Ruiz-Molina, D.; Wurst, K.; Domingo, N.; Cavallini, M.; Biscarini, F.; Tejada, J.; Rovira, C.; Veciana, J. *Nat. Mater.* **2003**, *2*, 190. (b) Maspoch, D.; Ruiz-Molina, D.; Veciana, J. *J. Mater. Chem.* **2004**, 2713 and references cited therein. (c) Kurmoo, M.; Kumagai, H.; Chapman, K. W.; Kepert, C. J. *Chem. Commun.* **2005**, 3012. (d) Rujiwatra, A.; Kepert, C. J.; Claridge, J. B.; Rosseinsky, M. J.; Kumagai, H.; Kurmoo, M. *J. Am. Chem. Soc.* **2001**, *123*, 10584. (e) Kurmoo, M.; Kumagai, H.; Hughes, S. M.; Kepert, C. J. *Inorg. Chem.* **2003**, *42*, 6709. (f) Halder, G. J.; Kepert, C. J.; Moubaraki, B.; Murray, K. S.; Cashion, J. D. *Science* **2002**, *298*, 1762. (g) Niel, V.; Thompson, A. L.; Munoz, M. C.; Galet, A.; Goeta, A. E.; Real, J. A. *Angew. Chem., Int. Ed.* **2003**, *42*, 3759. (h) Kepert, C. J. *Chem. Commun.* **2006**, 695.

(4) (a) Endo, T.; Akutagawa, T.; Noro, S.; Nakamura, T. *Dalton Trans.* **2011**, *40*, 1491−1496. (b) Akutagawa, T.; Sato, D.; Ye, Q.; Endo, T.; Noro, S.; Takeda, S.; Nakamura, T. *Dalton Trans.* **2010**, *39*, 8219−8227. (c) Akutagawa, T.; Sato, D.; Koshinaka, H.; Aonuma, M.; Noro, S.; Takeda, S.; Nakamura, T. *Inorg. Chem.* **2008**, *47*, 5951−5962. (d) Akutagawa, T.; Koshinaka, H.; Sato, D.; Takeda, S.; Noro, S. I.; Takahashi, H.; Kumai, R.; Tokura, Y.; Nakamura, T. *Nat. Mater.* **2009**, *8*, 342−347. (e) Akutagawa, T.; Shitagami, K.; Nishihara, S.; Takeda, S.; Hasegawa, T.; Nakamura, T.; Hosokoshi, Y.; Inoue, K.; Ikeuchi, S.; Miyazaki, Y; Saito, K. *J. Am. Chem. Soc.* **2005**, *127*, 4397−4402. (f) Rodríguez-Velamazán, J. A.; González, M. A.; Real, J. A.; Castro, M.; Muñoz, M. C.; Gaspar, A. B.; Ohtani, R.; Ohba, M.; Yoneda, K.; Hijikata, Y.; Yanai, N.; Mizuno, M.; Ando, H.; Kitagawa, S. *J. Am. Chem. Soc.* **2012**, *134*, 5083−5089.

(5) (a) Colacio, E.; Ghaze, M.; Kivekäs, R.; Moreno, J. M. *Inorg. Chem.* **2000**, *39*, 2882−2890. (b) Rodriguez-Martin, Y.; Ruiz-Pérez,

C.; Sanchiz, J.; Lloret, F.; Julve, M. *Inorg. Chim. Acta* **2001**, *318*, 159−165. (c) Ruiz-Pérez, C.; Sanchiz, J.; Hernandez-Molina, M.; Lloret, F.; Julve, M. *Inorg.Chem.* **2000**, *39*, 1363−1370 and references therein.

(6) (a) Cui, H. B.; Wang, Z. M.; Takahashi, K.; Okano, Y.; Kobayashi, H.; Kobayashi, A. *J. Am. Chem. Soc.* **2006**, *128*, 15074. (b) Jain, P.; Ramachandran, V.; Clark, R. J.; Zhou, H. D.; Toby, B. H.; Dalal, N. S.; Kroto, H. W.; Cheetham, A. K. *J. Am. Chem. Soc.* **2009**, *131*, 13625−13627. (c) Xu, G.-C.; Zhang, W.; Ma, X.-M.; Chen, Y.-H.; Zhang, L.; Cai, H.-L.; Wang, Z.-M.; Xiong, R.-G.; Gao, S. *J. Am. Chem. Soc.* **2011**, *133*, 14948−14951. (d) Tan, J.-C.; Jain, P.; Cheetham, A. K. *Dalton Trans.* **2012**, *41*, 3949−3952. (e) Pardo, E.; Train, C.; Liu, H.; Chamoreau, L.-M.; Dkhil, B.; Boubekuer, H.; Lloret, F.; Nakatani, K.; Tokoro, H.; Ohkoshi, S.; Verdaguer, M. *Angew. Chem., Int. Ed.* **2012**, *51*, 8356.

(7) (a) Yamazaki, Y.; Miyasaka, S.; Kaneko, Y.; He, J.-P.; Arima, T.; Tokura, Y. *Phys. Rev. Lett.* **2006**, *96*, 207204. (b) Scott, J. F. *J. Phys.: Condens. Matter* **2008**, *20*, 021001. (c) Eerenstein, W.; Mathur, N. D.; Scott, J. F. *Nature* **2006**, *442* (17), 759−765.

(8) Hagen, K. S.; Naik, S. G.; Huynh, B. H.; Masello, A.; Christou, G. *J. Am. Chem. Soc.* **2009**, *131*, 7516.

(9) Zhao, J.-P.; Hu, B.-W.; Lloret, F.; Tao, J.; Yang, Q.; Zhang, X.-F.; Bu, X.-H. *Inor. Chem.* **2010**, *49* (22), 10390−10399.

(10) Néel, L. *Ann. Phys. (Paris, Fr.)* **1948**, *3*, 137−198.

(11) (a) Nuttall, C. J.; Day, P. *Chem. Mater.* **1998**, *10*, 3050. (b) Mathonière, C.; Nutall, C. J.; Carling, S. G.; Day, P. *Inorg. Chem.* **1996**, *35*, 1201. (c) Carling, G. C.; Day, P.; Nuttall, C. J. *Spectrochim. Acta, Part A* **2001**, *57*, 1971.

(12) (a) Blasse, G.; Gorter, E. W. *J. Phys. Soc. Jpn., Suppl. B-1* **1962**, *17*, 176. (b) Gorter, E. W. *Philips Res. Rep.* **1954**, *9*, 403.

(13) Wilkinson, C.; Cowan, J. A.; Myles, D. A. A.; Cipriani, F.; McIntyre, G. J. *Neutron News* **2002**, *13*, 37.

(14) Rauch, H.; Waschkowski, W. Neutron Scattering Lengths. In *Neutron Data Booklet*; Dianoux, A.-J., Lander, G., Eds.; Institut Laue-Langevin: Grenoble, 2003; available on line at http://www.ill.eu.

(15) (a) Campbell, J. W. *J. Appl. Crystallogr.* **1995**, *28*, 228. (b) Campbell, J. W.; Hao, Q.; Harding, M. M.; Nguti, N. D.; Wilkinson, C. *J. Appl. Crystallogr.* **1998**, *31*, 496−502.

(16) Wilkinson, C.; Khamis, H. W.; Stansfield, R. F. D.; McIntyre, G. J. *J. Appl. Crystallogr.* **1988**, *21*, 471.

(17) Lehmann, M. S.; Larsen, F. K. *Acta Crystallogr.* **1974**, *A30*, 580.

(18) Campbell, J. W.; Habash, J.; Helliwell, J. R.; Moffat, K. *Information Quarterly for Protein Crystallography*, No. 18; SERC Daresbury Laboratory:Warrington, England, 1986.

(19) Sheldrick, G. M. *Acta Crystallogr.* **2008**, *A64*, 112−122.

(20) Duisenberg, A. J. M. *J. Appl. Crystallogr.* **1992**, *25*, 92−96.

(21) Spek, A. L. *Acta Crystallogr.* **2009**, *D65*, 148−155.

(22) (a) Richard, D.; Ferrand, M.; Kearley, G. J. *J. Neutron Res.* **1996**, *4*, 33−39. (b) LAMP, the Large Array Manipulation Program. http://www.ill.fr/data_treat/lamp/lamp.html.

(23) Coppens, P. *Crystallographic Computing*; Ahmed, F. R.,Ed.; Munksgaard International Booksellers and Publishers Ltd.: Copenhagen, 1979; pp 255−270.

(24) Howard, J. A. K.; Johnson, O.; Schultz, A. J.; Stringer, A.M. *J. Appl. Crystallogr.* **1987**, *20*, 120−122.

(25) *International Tables for Crystallograph. Vol. A, Space-Group Symmetry*; Hahn, T., Ed.; Wiley: Weinheim, Germany, 2006.

(26) Rodríguez-Carvajal, J. *Physica B* **1993**, *55*, 192. The programs of the FullProf Suite and their corresponding documentation can be obtained from the Web at http://www.ill.eu/sites/fullprof/.

(27) Bertaut, E. F.. In *Magnetism*; Rado, G. T., Shul, H.; Eds.; Academic: NewYork, 1963; Vol.*III*, Chap. 4.

(28) Rodríguez-Carvajal, J. *BasIreps: A program for calculating irreducible representation of little groups and basis functions of polar and axial vector properties*. Program included in the FullProf Suite, version July-2010, ILL, 2010.